




# Pressure-induced Anderson-Mott transition in elemental tellurium

Jaime F. Oliveira <sup>1✉</sup>, Magda B. Fontes<sup>1</sup>, Marcus Moutinho<sup>2</sup>, Stephen E. Rowley <sup>3</sup>, Elisa Baggio-Saitovitch<sup>1</sup>, Marcello B. Silva Neto<sup>4</sup> & Carsten Enderlein <sup>2✉</sup>

Elemental tellurium is a small band-gap semiconductor, which is always p-doped due to the natural occurrence of vacancies. Its chiral non-centrosymmetric structure, characterized by helical chains arranged in a triangular lattice, and the presence of a spin-polarized Fermi surface, render tellurium a promising candidate for future applications. Here, we use a theoretical framework, appropriate for describing the corrections to conductivity from quantum interference effects, to show that a high-quality tellurium single crystal undergoes a quantum phase transition at low temperatures from an Anderson insulator to a correlated disordered metal at around 17 kbar. Such insulator-to-metal transition manifests itself in all measured physical quantities and their critical exponents are consistent with a scenario in which a pressure-induced Lifshitz transition shifts the Fermi level below the mobility edge, paving the way for a genuine Anderson-Mott transition. We conclude that previously puzzling quantum oscillation and transport measurements might be explained by a possible Anderson-Mott ground state and the observed phase transition.

<sup>1</sup>Centro Brasileiro de Pesquisas Físicas, Rua Dr. Xavier Sigaud 150, Rio de Janeiro, RJ 22290-180, Brazil. <sup>2</sup>Campus Duque de Caxias, Universidade Federal do Rio de Janeiro, Rodovia Washington Luiz, Km 104,5, Duque de Caxias, RJ 25.240-005, Brasil. <sup>3</sup>Cavendish Laboratory, University of Cambridge, J J Thomson Avenue, Cambridge CB3 0HE, UK. <sup>4</sup>Instituto de Física, Universidade Federal do Rio de Janeiro, Rio de Janeiro, RJ Caixa postal 68528, Brazil. ✉email: [jaimedeoliveira@gmail.com](mailto:jaimedeoliveira@gmail.com); [carsten@caxias.ufrj.br](mailto:carsten@caxias.ufrj.br)

Elemental tellurium at ambient pressure is a small-band-gap semiconductor with a gap size  $\Delta \approx 330$  meV. Recently, the material and its allotropes received great attention: tellurium might possess Weyl-nodes within the valence band (VB)<sup>1</sup>, it has been proven to show extremely unusual direction-dependent magnetoresistance (interpreted as being due to the magnetochiral effect)<sup>2</sup>, it is considered to be an excellent thermoelectric<sup>3,4</sup>, its helices in nanotubes might help to extend Moore's law<sup>5</sup>, and its spin-texture allows a current-induced bulk magnetization<sup>6</sup>.

Due to a strong spin-orbit coupling (SOC), the top of the VB in tellurium has a double maximum and possesses a radial spin texture<sup>7,8</sup>. This is particularly important, since tellurium is naturally doped by vacancies, turning chemically pure samples into a *p*-type semiconductor exhibiting extrinsic resistivity curves<sup>9–11</sup>.

It is well established that under the application of hydrostatic pressure, tellurium's band gap narrows<sup>12</sup>, and the double maximum turns continuously into a single maximum between 15 and 20 kbar<sup>13</sup>. Recent density functional theory (DFT) calculations suggest transitions to topologically interesting phases below 30 kbar<sup>14,15</sup>. However, the only previous experimental study in the respective pressure range is at odds with a gap closing at a pressure below the crystal phase transition at 40 kbar<sup>16</sup>. On the other hand, a recent quantum oscillations study has been interpreted as being more consistent with these calculations<sup>17</sup>.

In our pressure-dependent study of the electrical transport properties of a high-quality tellurium single crystal, we find that the chemical potential enters the top of the VB when the temperature is lowered to around 1 K, which has been suggested previously<sup>13</sup>. Below this temperature and above a temperature at which the conductivity saturates, the material exhibits variable range hopping (VRH) behavior with the associated characteristic Mott-temperature scale  $T_0 \sim 10$  mK. Such a low  $T_0$  indicates that the hopping occurs between Anderson-localized states, of a rather large localization length. At about 17 kbar, the material undergoes a phase transition to a disordered metal ground state with characteristic  $\sqrt{T}$  dependence of the conductivity. Due to the SOC, again, the conductivity saturates at very low temperatures. The phase transition manifests itself in all measured and analyzed physical quantities and occurs at the critical pressure linked to the disappearance of the double maximum of the VB.

Naturally, the disappearance of the double maximum coincides with a Lifshitz transition, drastically changing the density of states (DOS) at the Fermi level. Consequently, the Fermi level passes through the mobility edge and the material demonstrates a quantum phase transition from an Anderson–Mott insulator to a disordered metal. Close to the critical point, the system exhibits a conductivity varying with temperature as  $\sigma \propto T^{1/3}$ . This is well known to be a signature of an Anderson–Mott-critical regime and is reminiscent of the universality between the Anderson–Mott transition in  $d = 3$  and random-field magnets<sup>18</sup>. Furthermore, the magnetoresistance changes from a VRH-typical negative magnetoresistance to a strong positive magnetoresistance as is the case for weakly anti-localized systems. The characteristic resistivity saturation at low temperature is a manifestation of the fact that at low temperatures the spin-orbit relaxation length exceeds the localization length. From the characteristic Mott temperature  $T_0$ , one can deduce the critical exponent of the correlation length. As the transition is related to the Anderson–Mott insulator-to-metal quantum critical point, all other critical exponents are correctly deduced from a straight-forward theoretical framework on the basis of quantum interference effects. To further illuminate the nature of the transition, we have performed DFT calculations, demonstrating the claimed Lifshitz transition, which ultimately coincides with the Anderson–Mott quantum critical point.

This study has identified and highlighted the importance of the quantum critical point in tellurium and provides an understanding of the ground state of high-purity tellurium crystals. It also addresses the intriguing theoretical predictions on the possible emergence of topologically interesting phases in chiral non-centrosymmetric tellurium. Furthermore, it demonstrates a unique scenario, in which pressure tunes an Anderson–Mott insulator-to-metal phase transition across a Lifshitz transition and therefore exhibits completely different characteristics from systems which undergo a true Lifshitz phase transition as in refs. 19,20.

## Results

**Semiconducting behavior.** Fig. 1a and b show how the resistivity  $\rho$  depends on the temperature  $T$ . One can see that for all measured pressures, the sample displays  $d\rho/dT < 0$  over the whole temperature range. The over-all resistivity curves are typical for an extrinsic semiconductor, which is consistent with studies of other high-purity tellurium samples (see for example, refs. 9–11,21). Above 150 K, over the whole pressure range, the sample exhibits intrinsic semiconductor behavior, which allows the extraction of the effective band gap between the conduction and the VB,  $\Delta$ , by applying the relation

$$\rho(T) \propto e^{-\frac{\Delta}{k_B T}}, \quad (1)$$

with  $k_B$  being the Boltzmann constant. The extracted pressure-dependent  $\Delta(P)$  is plotted in the inset in Fig. 1b. As shown in the figure, linear extrapolation of our data leads to a theoretical critical pressure for band closure above 40 kbar, in stark contrast to the relatively low pressure for band gap closure, which has been suggested by several other groups<sup>14,15,17</sup>. The data suggests that it is unlikely that tellurium undergoes a transition to a topologically insulating state or a Weyl semimetal before the crystal phase transition at 40 kbar. Our finding is consistent with previously published experimental results<sup>12,16,22</sup>.

## Anderson localization and disordered metallic behaviour.

When lowering the temperature, the resistivity behavior can no longer be described with the model associated with an intrinsic semiconductor. The entrance into the extrinsic regime is generally associated with the shift of the chemical potential, which at some point enters the impurity band, while the divergent resistivity close to zero temperature is normally associated with carrier freeze-out. However, in the case of a sufficiently high carrier density, the impurity band lowers and broadens until it hybridizes with the VB.

At low temperatures, we observe two anomalies at characteristic temperatures  $T_{a1}$  and  $T_{a2}$ , which we determined by the position of a local maximum in the first derivative of  $\rho(T)$ . For selected curves, the anomalies are marked in Fig. 1c and d by small black arrows (for a more detailed look on the resistivity data around the anomalies, see Supplementary Fig. 1). We believe the first anomaly to be the same, which has been reported before by Takita et al.<sup>10</sup> for chemically pure samples with low hole concentrations.

Below  $T_{a1}$  and above the temperature at which the conductivity approaches a saturated value  $\delta\sigma$  and below 16 kbar, the conductivity follows (see Fig. 1c)

$$\sigma(T) = \sigma_{\text{vrh}} \exp\left[-\left(\frac{T_0}{T}\right)^{\frac{1}{4}}\right], \quad (2)$$

which is typical for Mott-VRH behavior in three dimensions.

In Fig. 2a, we see the extracted values of  $T_0$ . This value of about 10 mK is at least five orders of magnitude lower than for doped

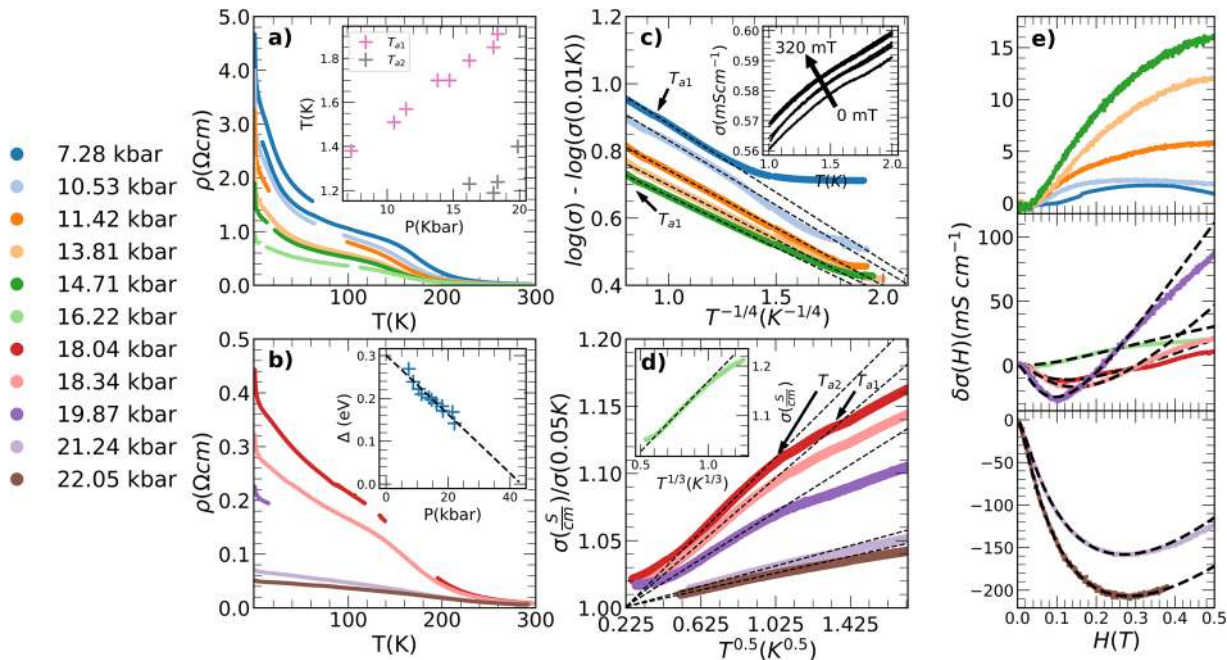


**Fig. 1 Transport and magnetotransport data.** **a** and **b**  $\rho(T)$  curves over the whole temperature and pressure range. Inset in **a**: characteristic temperatures of the two anomalies. Above 20 kbar, both anomalies seemingly disappear (or smear out). Inset in **b**: Development of the band gap with extrapolated fit. **c** Conductivity plots to demonstrate the VRH with  $\sigma \propto \exp(T_0/T)^{1/4}$ . The first anomaly is marked by small black arrows for two pressures. Inset: plot of the development of the anomaly under small magnetic fields at 13.81 kbar. **d** Conductivity plots to demonstrate  $\sigma \propto \sqrt{T}$ . Again, the two anomalies are marked by arrows for one pressure. Inset: Plot of the conductivity at 16.22 kbar. The  $\sigma \propto T^{1/3}$  law indicates critical behavior. **e** Magnetoconductance measurements at 500 mK for all pressures. In the lower and middle panel, curves are fitted by using the fitting function described by Eqs. (13) and (14).

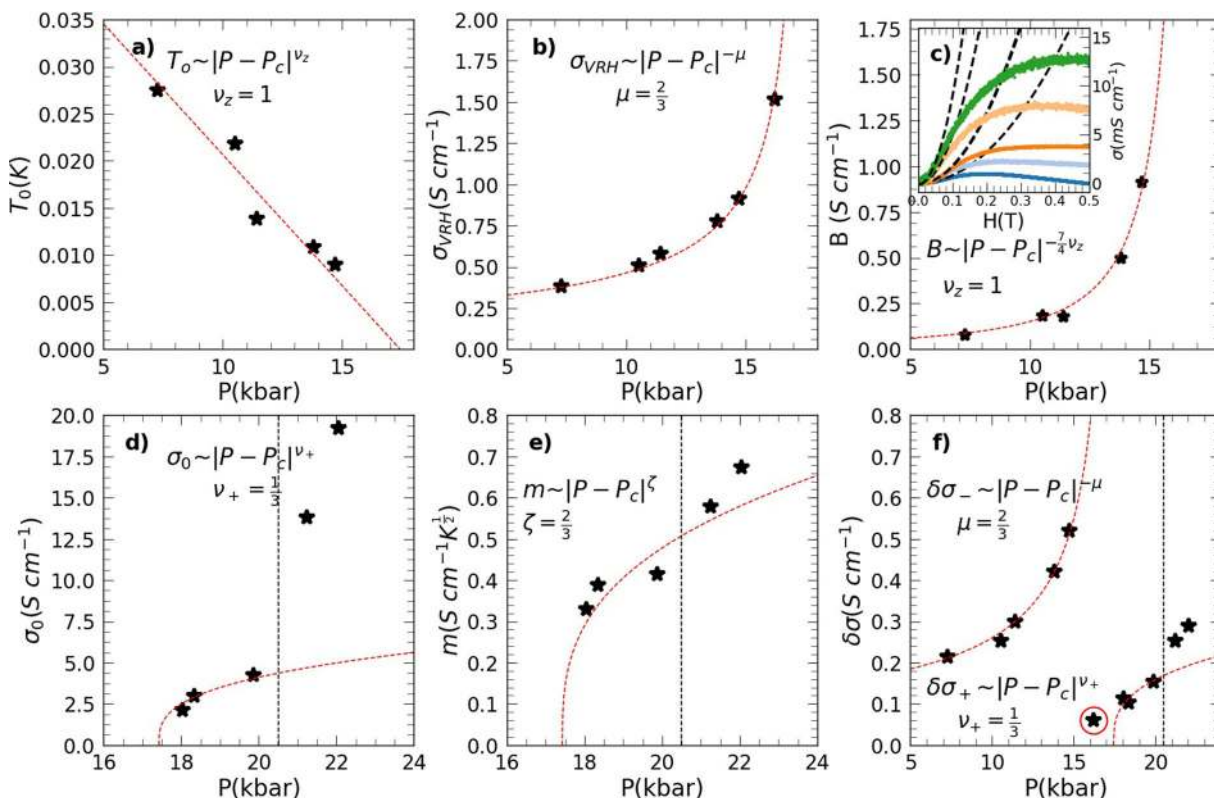


**Fig. 2 Characteristic physical quantities and how they either vanish or diverge.** The critical pressure is determined to be  $P_c = 17.43$  kbar. The red dashed lines represent fits with the mentioned critical pressure and critical exponents as they come out from the theory. The black dashed line represents the hypothetical Ioffe-Regel limit. The inset in panel **c** shows the 2K magnetoconductance data in the insulating phase to demonstrate the parabolic behavior at very low fields. The data point marked with a red circle in panel **f** refers to the critical regime. In the critical regime  $\delta\sigma$  does not fully vanish, as due to a Fermi energy  $\epsilon_F > 0$ , the spin-orbit relaxation length remains finite.



semiconductors, where the hopping occurs between localized donor or acceptor states. This is a strong indication that the hopping occurs between Anderson-localized states such as reported in refs. 23–26, which all exhibit a similarly low  $T_0$ . Therefore, we assume that the observed anomaly can be associated with the entrance of the Fermi level in the localized tails of the VB. This is consistent with the interpretation of the anomaly by Takita et al.<sup>10</sup> and with the kink in the resistivity curves of Averkiev et al.<sup>27</sup>, which can be found roughly at the same temperature but as the doping is higher, their sample demonstrates truly metallic behavior in the respective temperature range.

$T_{a1}$  increases with pressure, consistent with its association to the entrance of the chemical potential into the VB. Under the application of a magnetic field, the anomaly smears out, as shown in the inset of Fig. 1c. Again, this is consistent with the fact that it is associated with the entrance of the chemical potential into the band, as under the application of a magnetic field along the  $z$ -direction, the two band maximums degenerate.

At 16.22 kbar, the second anomaly appears. As will become clearer further below, this coincides with the entrance in the critical regime, where the camel-back shaped top of the VB, becomes a single maximum. Below the characteristic temperature  $T_{a2}$  at 16.22 kbar, the conductivity follows a  $T^{1/3}$ -behavior (see inset of Fig. 1d), which is characteristic for the critical regime of the Anderson–Mott transition<sup>28</sup>.

For higher pressures, the conductivity below  $T_{a2}$  follows:

$$\sigma = \sigma_0 + m \cdot \sqrt{T}, \quad (3)$$

with  $\sigma_0$  being the theoretical metallic zero temperature conductivity and  $m$  being a characteristic quantity. Therefore, we conclude that the second anomaly is associated with the passing of the chemical potential through the mobility edge, as this low temperature resistivity behavior has been associated with disordered metals<sup>29</sup>.

In the upper panel of Fig. 1e, we see the magnetoconductance data at 500 mK in the insulating regime. We see a small feature of positive magnetoconductance at very low fields, which can very likely be associated with weak-antilocalization (WAL), due to SOC. Above the critical pressure, there is a strong change in magnetoconductance with a pronounced WAL feature.

**Critical behaviour and the quantum phase transition.** From our data, we extract six characteristic quantities to describe the previously discussed behavior: The characteristic temperature  $T_0$  and the prefactor  $\sigma_{vrh}$  from VRH, the prefactor of the parabolic magnetoconductance behavior at low fields, the difference between the extrapolated zero temperature conductivity and the saturation conductivity  $\delta\sigma$ , and  $m$  and  $\sigma_0$  from the quantum interference conductivity. Their pressure dependence is plotted in Fig. 2. Before extensively discussing the results in the next section, we point out that the data suggests that all of these either diverge or disappear at a critical pressure of 17.43 kbar.

The respective Mott–Anderson transition coincides with the pressure-induced Lifshitz transition in  $p$ -type tellurium<sup>13,17</sup>. As will be established below, at the point of the Lifshitz transition the Fermi level is pushed below the mobility edge, leading to an Anderson–Mott quantum critical point. The Lifshitz transition is illustrated in Fig. 3d–i, which exhibits the results from DFT calculations considering SOC in tellurium systems with different lattice parameters. Due to the interplay of van-der-Waals and covalent forces, band calculations of tellurium differ strongly among different groups. However, as we are only interested in the well-established qualitative change of the top of the VB, we believe that our qualitative statements remain valid.

In Fig. 3g–i, we see the structure of the top of the tellurium VB around the H-point for three different pressures. The Fermi level refers to a theoretical charge carrier density of  $1 \times 10^{16} \text{ cm}^{-3}$ . This value is two orders of magnitude higher than the one we have measured by Hall. However, as the calculations serve mainly an illustrative purpose (meaning: they show the existence of a Lifshitz transition), we chose to use a higher charge carrier density. If we had used the measured charge carrier density, the necessary resolution for the DFT calculation would simply be too high to justify the time of calculation and moreover, the actual change of topology of the Fermi surface would be much more difficult to visually access in the figure. In Fig. 3d–f, we see the respective cuts through  $k$ -space with the respective Fermi surface cross-sections and the related spin texture. Fig. 3e and h represent the critical pressure at which one identifies the Lifshitz transition. One can recognize immediately how the spin texture qualitatively explains that the WAL feature is much more pronounced on the metallic side (the side with one closed Fermi surface). On the insulating side mainly two opposite spin directions exist and the magnetic field cannot easily lift the suppressed enhanced backscattering, while on the metallic side of the transition this can occur easily for a relatively huge fraction of the charge carriers as the strength of the spin polarization is significantly lower.

## Discussion

All measured quantities presented above and discussed below indicate that the insulator–metal transition (IMT) is of the Anderson–Mott manifold<sup>18</sup>. However, differently from most cases, where the tuning parameter for such a transition is the dopant density<sup>30</sup>, here the tuning parameter is the hydrostatic pressure. The transition occurs for a constant dopant density and a pressure-induced Lifshitz transition, which pushes the chemical potential below the mobility edge, paving the way for an Anderson–Mott IMT, as shown in Fig. 3. This can be easily visualized, when visually comparing the Fermi energies between Fig. 3g and i.

As the data suggests and the following theory further corroborates, an Anderson–Mott IMT does indeed occur around the critical pressure associated with the Lifshitz transition, where the Fermi surface changes its topology. Thus we shall name this transition a Lifshitz–Anderson–Mott transition (LAMT). It is important to note that, although the transition occurs due to a topological change of the Fermi surface, it is actually of the Anderson–Mott manifold and obeys all its universal characteristics. This becomes particularly clear, when recognizing that on both sides of the transition, transport is clearly dictated by quantum interference corrections and in the critical regime, the Anderson–Mott typical  $\sigma = \sigma_0 + AT^{1/3}$  is observed. The universality between the Anderson–Mott transition in  $d=3$  and random-field magnets<sup>18</sup> allows us to identify the dynamic exponent  $z$ , from the  $AT^{1/z}$  critical behaviour which, according to Wegner’s scaling,  $z = \beta\delta/\nu$ , for  $\beta = \nu$  and  $\delta = 3$ <sup>18</sup>, should be fixed to  $z = 3$ , in agreement with our data, and markedly different from the  $z = 4$  exponent expected from a true Lifshitz phase transition. Furthermore, as the bandwidth scales roughly linearly with pressure, we would expect the closeness to the mobility edge also scales linearly with pressure and therefore there is no overlying critical dependence from the true Lifshitz transition.

To fully establish the nature of the LAMT, we now describe the transport properties of elemental tellurium within the framework of the relative corrections to conductivity,  $\delta\sigma$ , arising due to quantum interference effects. As it will become clear shortly, this framework is found to be valid throughout the entire phase diagram: from the insulating (hopping), through the critical (bad metal/bad insulator), and up to the metallic (diffusive) regimes.

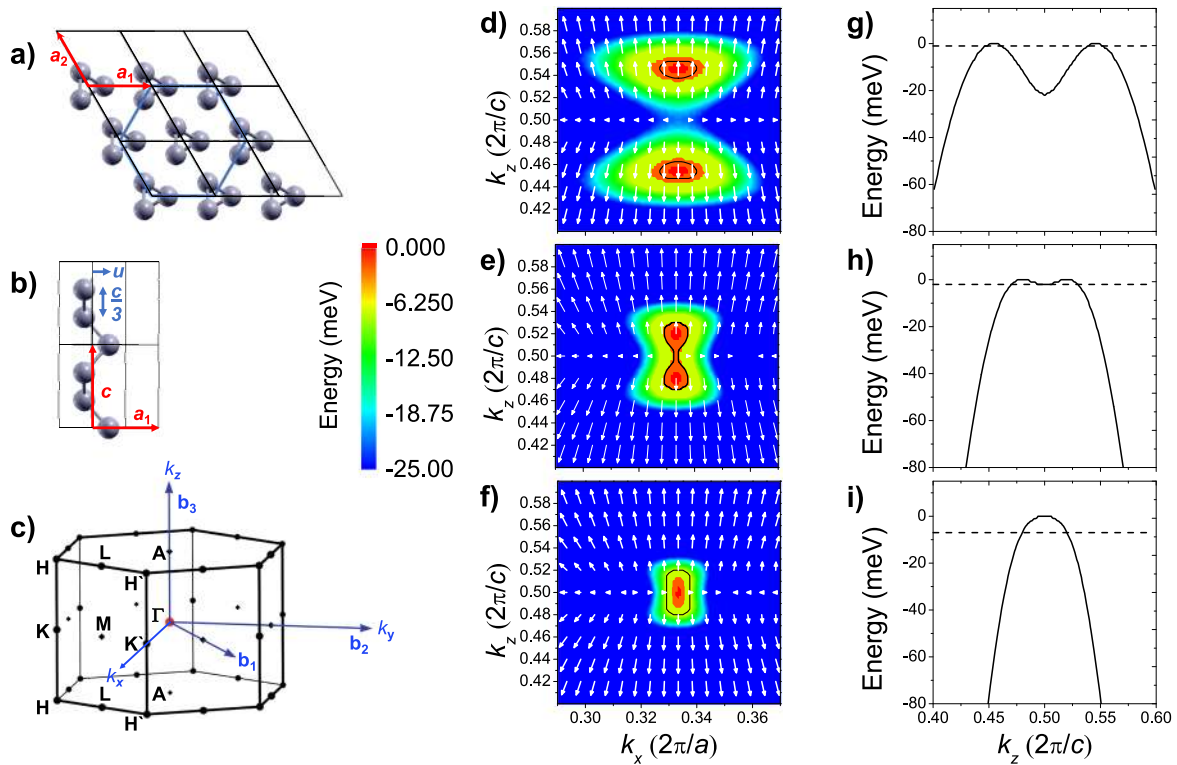


**Fig. 3** Theoretical calculations of the band structure and the spin texture around the H-point for different pressures. **a** and **b** Schematic representation of the tellurium atomic structure with the hexagonal Bravais lattice vectors,  $\mathbf{a}_1$ ,  $\mathbf{a}_2$  and  $\mathbf{c}$  and the internal atomic position parameter  $u$ . The three tellurium atoms are placed at  $(u, 0, 0)$ ,  $(0, u, 1/3)$  and  $(-u, -u, 2/3)$  in units of the crystal lattice. **c** Reciprocal lattice ( $\mathbf{b}_1$ ,  $\mathbf{b}_2$ , and  $\mathbf{b}_3$ ) and cartesian ( $k_x$ ,  $k_y$ , and  $k_z$ ) direction vectors of the hexagonal Bravais lattice as well as the special points. **d-f** Two-dimensional plot of the valence band in the  $k_x \times k_z$  plane together for three pressure points:  $P < P_c$  (subfigure **d**),  $P \approx P_c$  (subfigure **e**), and  $P > P_c$  (subfigure **f**) (further information in Supplementary Note 1). The white arrows display the calculated spin texture. The black line represents the Fermi contour for a hypothetical charge carrier density of  $10^{16} \text{ cm}^{-3}$ . **g-i** Electronic energy dispersion of the valence band along of the K-H-K path of the Brillouin Zone for the same pressure points. The dashed line represents the Fermi energy for the same charge carrier density.

For  $P < P_c$ , the system is in the insulating regime, where all electrons are strongly localized and their wavefunctions fade away within distances of the order of the localization length,  $\xi_L$ . In this case, the conductivity is determined by the exponential tails of the wavefunctions,  $\sigma(T) \propto \exp\{-L_\varphi(T)/\xi_L\}$ , and its temperature dependence is set by the inelastic dephasing length  $L_\varphi(T) \sim \sqrt{\tau_\varphi(T)}$ . The inelastic scattering time,  $\tau_\varphi(T)$ , in turn, is calculated from the inverse transition rate,  $\tau_\varphi \sim \Gamma^{-1}$ , via Fermi's golden rule as  $\Gamma \sim \int dR R^2 \int d(\Delta\epsilon) |M|^2 \exp\{-2R/\xi_L - \Delta\epsilon/k_B T\}$ , where  $M$  is the pre-exponential factor. Now, if phase coherence is destroyed over optimal hopping distances,  $R \sim \bar{r}$ , that are usually accompanied by large energy variations,  $\Delta\epsilon \gg k_B T$ , then one must include a constraint connecting  $\bar{r}$  to  $n(\epsilon_F)$ , the density of randomly distributed states per volume per energy,  $\bar{r}^d n(\epsilon_F) \sim \text{const}$ . In this case one finds  $L_\varphi \sim T^{-b}$ , with  $b = 1/(d+1)$ , and, at low temperatures, one obtains Mott's VRH law (eq. (2))<sup>31</sup>, which is therefore characterized by two quantities: the pre-exponential conductivity

$$\sigma_{\text{vrh}}(\bar{r}) = e^2 n(\epsilon_F) \nu_{\text{ph}} \bar{r}^2, \quad \text{and} \quad T_0(\xi_L) = \frac{4\nu_c}{k_B n(\epsilon_F) \xi_L^3}, \quad (4)$$

the Mott temperature<sup>32</sup>. Here,  $e$  is the elementary charge,  $\nu_{\text{ph}}$  is a measure of the (constant) phonon density of states and  $\nu_c$  is a geometrical constant of the order of unity associated with the percolating hopping network of random resistors<sup>32</sup>. As

demonstrated in Fig. 1c, for  $P < P_c$ , we observe clear VRH behavior from which we can extract the evolution of the above two quantities,  $T_0$  and  $\sigma_{\text{vrh}}$ , as a function of pressure, as the LAMT is approached from the left (displayed in Fig. 2a and b, respectively).

Concerning the evolution of Mott temperature,  $T_0(P)$ , let us remark that the anisotropic envelope wave-function of acceptors in tellurium can be written as  $\psi(x, y, z) \sim \exp\{-\sqrt{(x^2 + y^2)/\xi_{xy}^2 + z^2/\xi_z^2}\}$ . As a result, in the expression for Mott's temperature in Eq. (4) one should actually replace  $\xi_L^3 \rightarrow \xi_{xy}^2 \xi_z$ <sup>33</sup>. As demonstrated in Fig. 2a, our data suggests that  $T_0$  vanishes linearly with the distance to the LAMT critical point,  $T_0 \sim |P - P_c|$ . Since in tellurium, the LAMT is dominated by the divergence of  $\xi_z$  with pressure

$$\xi_z \sim |P - P_c|^{-\nu_z}, \quad (5)$$

while  $\xi_{xy}$  is somewhat robust and remains finite across the transition, the linearity of  $T_0$  thus implies that  $\nu_z = 1$ . As a result, the localization length of acceptors,  $\xi_L = (\xi_{xy}^2 \xi_z)^{1/3}$ , should diverge with a critical exponent  $\nu = \nu_z/3 = 1/3$ .

Analogously, the divergence of the pre-exponential conductivity,  $\sigma_{\text{vrh}}$ , as  $P \rightarrow P_c$ , should be associated, according to universality, to the divergence of the static dielectric polarizability,  $\chi$ <sup>30,34</sup>. Indeed, when transport occurs via hopping, the static polarizability is proportional to the square of the optimal hopping distance,  $\chi \propto \bar{r}^2$ , which becomes the appropriate measure of the oscillator strength within the insulator. Now, if we

recall that in Mott's law the pre-exponential  $\sigma_{\text{vrh}}(\bar{r}) \sim \bar{r}^2$ , we conclude that  $\sigma_{\text{vrh}} \propto \chi$ . Furthermore, for interacting electrons  $\chi \sim \xi_L^2$ <sup>34</sup> and we thus conclude that the pre-exponential conductivity should diverge as,  $\sigma_{\text{vrh}} \sim |P - P_c|^{-2/3}$ , as indeed observed in Fig. 2b. For further universality arguments fixing all the above critical exponents see Supplementary Notes 4, 5, and Supplementary Fig. 6.

Surprisingly, however, the data fitted with Mott's VRH  $\exp\left\{-\left(T_0/T\right)^{1/4}\right\}$  law points towards saturation of the conductivity as  $T \rightarrow 0$  (see Fig. 1c), in clear contradiction with a true insulating ground state. Concerning the origin of such conductivity saturation, we can rule out possible self-heating, finite-size effects, and deem it unlikely to originate from a surface state as described by Li and Appelbaum<sup>35</sup> (for a deeper discussion on these points, we refer to Supplementary Note 3). Alternatively, we recall that conductivity saturation does occur naturally in insulators with spin-orbit interaction, since it delocalizes electrons when their localization length,  $\xi_L$ , becomes comparable to the associated spin-orbit relaxation length,  $L_{\text{s.o.}}$ . As discussed in detail in the Supplementary Note 4, this occurs due to a shift of the mobility edge, for  $\xi_L \sim L_{\text{s.o.}}$ , towards the top of the VB<sup>36,37</sup>. Now phase coherence is destroyed over non-optimal hopping distances,  $R \sim L_{\text{s.o.}}$ , that are, instead, associated to a thin energy layer of thickness  $\Delta\epsilon \sim k_B T$  around the Fermi level<sup>38</sup>, and one concludes that  $L_\varphi \sim L_{\text{s.o.}} \sim \sqrt{\tau_{\text{s.o.}}}$ . Since spin-flip scattering time does not depend on the temperature, we conclude that non-optimal hopping transport produces a correction to the conductivity below  $P_c$  given by

$$\delta\sigma_-(T \rightarrow 0) = \sigma_{\text{vrh}}(L_{\text{s.o.}}^2), \quad (6)$$

which shows saturation at the lowest temperatures  $\sigma(T \rightarrow 0) \neq 0$ , and, in this case, the ground state, even for  $P < P_c$ , becomes truly delocalized due to the spin-orbit interaction, with  $\delta\sigma(P \rightarrow P_c)$  diverging with the same critical exponent as  $\sigma_{\text{vrh}}$ , when  $L_{\text{s.o.}}(P \rightarrow P_c) \sim \xi_L(P \rightarrow P_c) \rightarrow \infty$  (see Fig. 2f).

For  $P > P_c$ , the material is in the so-called disordered metallic (diffusive) regime. The conductivity,  $\sigma(T) = \sigma_0 + m\sqrt{T}$ , in such weak-localization diffusive regime should then be fully characterized by two quantities, when represented as a straight line in a  $\sigma(T) \times \sqrt{T}$  plot: a small  $T \rightarrow 0$  intercept,  $\sigma_0$ , and a constant slope,  $m$ . Surprisingly, however, the data shown in Fig. 1d is characterized by a  $T \rightarrow 0$  intercept that is larger than the expected  $\sigma_0$ . This occurs in disordered metals with strong SOC when the main dephasing mechanism at low temperatures becomes dominated by spin-flip scattering,  $\tau_\varphi \rightarrow \tau_{\text{s.o.}}$ . In this case, and recalling that  $\tau_{\text{s.o.}}$  is temperature independent, one expects a saturation of the conductivity above  $P_c$  as the temperature is further reduced

$$\delta\sigma_+(T \rightarrow 0) = \frac{e^2}{h} \frac{1}{L_{\text{s.o.}}}, \quad (7)$$

and the correction to the conductivity becomes a direct measure of the spin-orbit relaxation length,  $L_{\text{s.o.}} \sim \sqrt{\tau_{\text{s.o.}}}$ <sup>39</sup>. This is indeed what Fig. 1d shows: a clear deviation from the  $\sqrt{T}$  law as  $T \rightarrow 0$  towards saturation.

Before we proceed to the analysis of the slope  $m$ , let us remark on a fundamentally important universality between Eqs. (6) and (7). As demonstrated by Götze<sup>40</sup>, or simply by using consistent dimensionality arguments, one sees that the divergence of a localization length scale squared,  $\xi_L^2$ , which enters the saturation conductivity within the insulator,  $\delta\sigma_- \propto \sigma_{\text{vrh}} \propto \chi \sim \xi_L^2$ , as  $P \rightarrow P_c^-$ , is the counterpart to the divergence of a correlation length,  $\xi$ , which enters the saturation conductivity within the

metal,  $\delta\sigma_+ \sim \xi^{-1}$ , as  $P \rightarrow P_c^+$ . This may be expressed as

$$\delta\sigma_-(P \rightarrow P_c^-) \propto \frac{1}{\delta\sigma_+(P \rightarrow P_c^+)}. \quad (8)$$

Thus, once the critical exponent of either one of these two quantities is determined, the corresponding counterpart is immediately fixed. Indeed, we have found previously that  $\xi_L$  diverges with an exponent  $\nu_- = 1/3$ . According to universality, this should be the same critical exponent for the correlation length,  $\xi \sim |P - P_c|^{-\nu_+}$ , at the metallic side of the transition,  $\nu_+ = \nu_- = 1/3$ . Since  $\delta_+\sigma \sim 1/\xi$  above  $P_c$  and since according to Götze  $\delta\sigma_- \propto 1/\delta\sigma_+$ <sup>40</sup>, one concludes that  $\delta\sigma_- \propto \sigma_{\text{vrh}} \sim |P - P_c|^{-\mu}$  should diverge at the transition with a critical exponent of  $\mu = 2\nu_+ = 2/3$ . This is exactly what one obtains from the experimental data within the insulating regime,  $P < P_c$ . We have verified that the above universality extends from the insulating, through the critical, up to the diffusive metallic regimes, including the divergence of  $\sigma_0 = (e^2/h)\xi^{-1}$ , with exponent  $\nu_+ = 1/3$ , as seen in Fig. 2d, breaking, however, beyond the Ioffe-Regel limit  $k_F\ell = 1$ , with  $\ell$  being the electronic mean free path of the diffusive, metallic phase, where  $\sigma_0 = (e^2/h)(k_F\ell)^2/\ell$ , and the scaling of  $\delta\sigma_+$  with pressure is no longer governed by  $\xi$ .

Returning now to the analysis of the  $\sigma(T) = \sigma_0 + m\sqrt{T}$  conductivity, one observes that the slope,  $m$ , is not constant, but exhibits a marked dependence on pressure,  $m(P)$ , vanishing precisely at the critical point of the LAMT (Fig. 2e). We were able to trace this back to the competition between exchange and Hartree contributions to the conductivity, as pressure is varied. Indeed, when further corrections due to interactions, disorder, anisotropies, and multi-valley structure in low-temperature semiconductors in  $d=3$  are taken into account<sup>39</sup>, the slope

$$m = 0.915 \times S_0 \times \left(\frac{e^2}{h}\right) \left(\frac{1}{4\pi^2}\right) \left(\lambda^{(j=0)} - \frac{3}{2}\gamma\lambda^{(j=1)}\right) \sqrt{\frac{1}{hD}}. \quad (9)$$

Here  $\lambda^{(j=0)} = 4/d$  is the exchange contribution due to electron-hole pairs (diffusion) in the singlet channel with total spin  $j=0$ , while  $\lambda^{(j=1)} = 32/(d(d-2))[1 + dF/4 - (1 + F/2)^{d/2}]/F$ , for  $d=1,3$  with  $F = 2\ln(1+x)/x$ , and  $x = 4k_F^2/\kappa^2$  ( $\kappa$  being the Thomas-Fermi screening wavenumber, or inverse screening length), is the sum of the three Hartree contributions due to electron-hole pairs (diffusion) in the triplet channel with total spin  $j=1$ , each carrying a weight of 1/2 (the coefficient 3/2 being thus connected to the multiplicity  $m=2j+1$  of the  $j=1$  state)<sup>39</sup>. The factor  $S_0$  accounts for valley anisotropies<sup>41</sup>. All other effects, such as the intravalley scattering, anisotropies in the dielectric (screening) properties, or yet the spin-orbit interaction, are known to modify the Hartree terms only,  $\lambda^{(j=1)}$ , reducing it with respect to the more robust, unaltered, and dominant exchange contribution,  $\lambda^{(j=0)}$ . This is encoded into a single renormalization parameter  $\gamma < 1$  for the Hartree contribution.

In elemental tellurium, one observes that  $m(P > P_c) > 0$ , since the exchange is always larger than the Hartree contributions,  $\lambda^{(j=0)} > \lambda^{(j=1)}$ . Nevertheless, one also observes that  $m$  vanishes at the Lifshitz point  $m(P \rightarrow P_c) \rightarrow 0$ , which implies that  $\lambda^{(j=0)} - (3/2)\gamma\lambda^{(j=1)}(P \rightarrow P_c) = 0$ . This occurs exactly at the point where the Fermi surface goes through a reconstruction, a topology change, and thus  $k_F(P \rightarrow P_c) \rightarrow 0$  or  $x(P \rightarrow P_c) \rightarrow 0$ , exactly where  $F$  is maximal. Let us then set  $\gamma = (8/9)(\lambda^{(j=1)}(P \rightarrow P_c))^{-1}$ , and expand  $m$  around  $x=0$  to obtain  $m(P \rightarrow P_c) \sim (k_F^2/\kappa^2)$ . The Lifshitz transition occurs for a correlation length,  $\xi$ , that becomes comparable to the average distance between electrons,  $1/k_F$ . In other words,  $k_F \sim 1/\xi$ . As a result we conclude that, since in elemental tellurium the exponent of the correlation length is  $\nu = 1/3$ , the coefficient  $m$  of the  $\sqrt{T}$  term in the conductivity should scale as



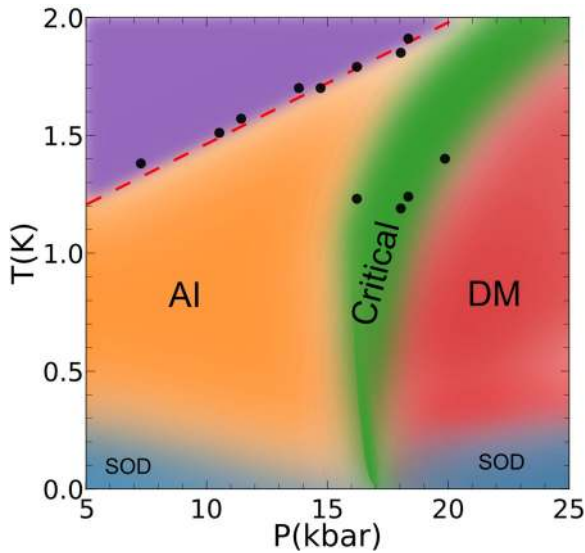


**Fig. 4 Speculative phase diagram of the LAMT in tellurium.** The violet area represents the area, where the chemical potential is not situated in the band. AI: Anderson insulator ( $L_{s.o.} > \xi_L$ ). SOD: spin-orbit delocalization. DM: disordered metal. The green area represents the critical regime. The black circles mark the positions of the anomalies, which coincide with the temperature to which VRH and/or  $\sigma = \sigma_0 + A \cdot T^b$  is a good fit. Thus, the red dashed line marks roughly the temperature at which we expect that the fermi level enters the localized states of the valence band.

$m \sim k_F^2 \sim 1/\xi^2 \sim |P - P_c|^{2/3}$ , in agreement with the data shown in Fig. 1e.

Finally, for  $P \sim P_c$ , and/or in the opposite limit of higher temperatures, one arrives at the critical (bad metal/bad insulator) regime. In this regime, the electron diffusion becomes comparable to the inelastic dephasing length,  $L_\varphi = \sqrt{D\tau_\varphi}$ , and, as a result, the diffusion coefficient,  $D$ , acquires a  $T$  dependence as determined by Einstein's relation,  $\sigma(T) = e^2 N(\epsilon_F) D(T)$ , where  $N(\epsilon_F)$  is the electronic density of states at the Fermi level. The scaling of the conductivity with temperature then crosses over to<sup>42</sup>

$$\sigma(T) = \sigma_0 + \beta T^{1/3}, \quad (10)$$

with  $\sigma_0 = (e^2/h)\xi^{-1}$  and  $\beta = (e^2/h)N(\epsilon_F)^{1/3}$ , characterizing the weak-localization critical regime. This is exactly what can be observed in the inset of Fig. 1d, for  $P \sim P_c$ .

Next we shall consider the magnetic field dependence of  $\delta\sigma$ . Here, quantum interference also governs the magneto-transport properties in elemental tellurium throughout the entire phase diagram. For  $P < P_c$  the relative corrections to the conductivity associated to quantum interference effects arising between the possible different paths for variable range hopping is described by<sup>43</sup>

$$\frac{\delta\sigma_-(H)}{\sigma(0)} \sim \frac{\int_{\sigma(0)/\sigma_{vrh}}^{\infty} [\ln(z\sigma(0)/\sigma_{vrh})]^{2d+2} [F_H(z) - F_0(z)] dz}{[\ln(\sigma_{vrh}/\sigma(0))]^{2d+1}}, \quad (11)$$

and the functions  $F_0(z)$  and  $F_H(z)$  are given in ref. 43. At low enough fields, the numerator of Eq. (11) gives us  $\delta\sigma_-(H) \sim [(\sigma_{vrh}/\sigma(0))^{I_{3/2}} - I_{1/2}]H^2$  and the magneto-conductance is quadratic with a sign that can be either positive or negative, depending on the ratio  $\sigma_{vrh}/\sigma(0)$ . A positive quadratic behavior for the magnetoresistance in elemental tellurium at small fields,  $\delta\sigma_-(H)/\sigma(0) \sim BH^2$  with  $B > 0$ , can be clearly seen in the upper panel of Fig. 1e, which corresponds to the insulating (hopping) regime,  $P < P_c$ . However, at low temperatures, even in the insulating phase, as

previously mentioned, the magnetoconductance displays a quantum interference contribution in form of WAL features at very low fields. Therefore, the divergence of the coefficient  $B$  is better analyzed using our magnetoconductance curves at 2 K (see inset Fig. 2c), where the quantum spin-orbit-induced WAL is less predominant. The respective curves are displayed in Fig. 2c and as  $P \rightarrow P_c^-$ ,  $B(P)$  is governed, in turn, by the denominator of Eq. (11)<sup>43</sup>

$$B(P \rightarrow P_c^-) \sim \left[ \ln \left( \frac{\sigma_{vrh}}{\sigma(0)} \right) \right]^{-(2d+1)} \sim \xi_L^{3(2d+1)/(d+1)}, \quad (12)$$

for  $\sigma(0) \equiv \sigma(T, H = 0) = \sigma_{vrh} \exp\left\{- (T_0/T)^{1/(d+1)}\right\}$  and  $T_0 \sim \xi_L^{-3}$ . Since  $\xi_L \sim |P - P_c^-|^{-\nu_-}$ , we obtain  $B \sim |P - P_c^-|^{-3\nu_-(2d+1)/(d+1)}$ . As a result, the magnetotransport within the insulating regime, and at small fields, is characterized by a quadratic coefficient,  $B$ , that diverges with a critical exponent equal to  $3\nu_-(2d+1)/(d+1) = 7/4$ , in  $d=3$  (and recalling that  $\nu_- = 1/3$ ), in agreement with the data shown in Fig. 2c.

For  $P > P_c$ , the corrections to conductivity in the disordered metallic (diffusive) regime in the presence of a magnetic field are given by<sup>41</sup>

$$\delta\sigma_+(H) \sim \frac{e^2}{h} \frac{1}{2\pi^2} \left( \frac{eH}{h} \right)^{d/2-1} \left\{ \frac{3}{2} f_d \left( \frac{H}{H_{s.o.}} \right) - \frac{1}{2} f_d \left( \frac{H}{H_\varphi} \right) \right\}, \quad (13)$$

$H_\varphi = (\hbar c/4eD)\tau_\varphi^{-1}$  and  $H_{s.o.} = (\hbar c/4eD)(\tau_\varphi^{-1} + 4\tau_{s.o.}^{-1}/3)$ . Once again, at high enough temperatures  $\tau_\varphi^{-1} \gg \tau_{s.o.}^{-1}$ , one ends up with a single Kawabata function which in  $d=3$  behaves like  $f_3(x) \sim x^{3/2}$  for  $x \ll 1$  and  $f_3(x) \sim \text{const}$  for  $x \gg 1$ . One would thus expect the magneto-conductance to be positive, behaving as  $H^2$  at low fields, while exhibiting a  $\sqrt{H}$  behavior at large fields in  $d=3$ . However, at lower temperatures  $\tau_{s.o.}^{-1}$  can no longer be ignored and the magneto-conductance changes sign due to anti-localization effects associated to the spin-orbit interaction. This is seen in both the middle and lower panels of Fig. 1e, which correspond, respectively, to the nearly critical and highly diffusive metallic regimes.

Furthermore, for the particular case of tellurium, it has been shown by Averkiev et al. 27 that the magneto-conductance is better fitted provided we replace

$$-\frac{1}{2} f_d \left( \frac{H}{H_\varphi} \right) \rightarrow f_d \left( \frac{H}{H_\nu} \right) + \frac{1}{2} f_d \left( \frac{H}{H_\nu} \right) - \frac{1}{2} f_d \left( \frac{H}{H_\varphi} \right), \quad (14)$$

and, for the case  $d=3$ , the function  $f_3(x)$  can be found in ref. 44. As shown in Fig. 1e, the magnetoconductance can be fitted very well with this function. Unfortunately, the structure of the function includes that the characteristic fields  $H_\nu$  and  $H_\varphi$  cannot be very well determined by a fit, as they are highly correlated. However, we can meaningfully extract the proportionality factor from the magnetoconductance fitting function and  $H_\varphi$ , at least for the highest two pressures 21.04 and 22.05 kbar (for details see Supplementary Figs. 3–5, Supplementary Tables 1–7, and Supplementary Note 2). For both of these pressures,  $H_\varphi$  increases linearly with temperature, as one would expect from dephasing from Johnson-like thermal fluctuations. When assuming that

$$H_\varphi(T) = A_\varphi T, \quad (15)$$

we determine and  $A_\varphi = 4.8$  and  $5.8$  mT/K for 22.05 and 21.24 kbar, respectively. For plots and a slightly deeper discussion (see Supplementary Note 2 and Supplementary Fig. 5).

Our considerations lead to a speculative phase diagram, as demonstrated in Fig. 4 (black circles represent the positions of the anomaly, which coincides with the respective change of slope in the  $R-T$  curves). Two different effects lead to the critical range

displaying a pressure dependence: on the one hand, as can be seen in Fig. 3, the Fermi energy shifts quicker on the metallic side of the transition. On the other hand, the pressure-induced bandwidth enhancement leads to the critical regime being shifted to higher pressures for comparably high temperatures. The low temperature delocalized spin-orbit phase has been determined by rough optical estimation.

Finally, we would like to discuss an apparent inconsistency: the charge carrier density from Hall measurements was determined to be around  $6 \times 10^{14} \text{ cm}^{-3}$ . This leads to an average distance of vacancies of roughly 100 nm. To have delocalized states with such low carrier concentration would suggest a dielectric constant of about 1000, while the literature suggests a room temperature dielectric constant in the order of 50<sup>45</sup>. However, this actual delocalization of acceptor states is common in the literature: Bresler et al.<sup>46</sup> and von Klitzing and Landwehr<sup>47</sup> measure a clear Fermi surface at ambient pressure at charge carrier densities of  $3 \times 10^{15} \text{ cm}^{-3}$  and around  $10^{14} \text{ cm}^{-3}$ , respectively. This has led to the idea that there exists an accumulation layer close to the surface, which von Klitzing and Landwehr related to their surface treatment. However, the dielectric constant naturally diverges at an Anderson–Mott transition and, therefore, we would expect the dielectric constant to be much higher in the low temperature range and further increase under pressure. This is also supported by historical measurements<sup>48</sup>.

One should mention that Rikken's results<sup>2</sup> suggest that Hall measurements on tellurium might lead to wrong conclusion, due to a non-trivial magnetoelectric response function.

Our data combined with our theoretical considerations strongly suggest the existence of a LAMT under the application of modest pressure in high purity tellurium single crystals. The well-established pressure-induced band bending leads to a change from the double-maximum camel-back like top of the VB to a single maximum. In samples with low carrier concentrations the related Lifshitz point will naturally coincide with a transition from an Anderson–Mott insulator to a disordered metal. The localization length diverges in only one direction (which coincides with the direction related to the neck-disrupting Lifshitz point or the divergent direction of the effective mass tensor). However, due to the strong spin polarization, the charge carriers remain delocalized at very low temperatures due to the temperature-independent spin-orbit relaxation length. The identification of this transition is of great consequence for the interpretation of many puzzling experimental results.

The anomaly, first observed by Takita et al.<sup>10</sup> arises from the entrance of the chemical potential in the Anderson–Mott localized tail of the VB. This is consistent with their explanation in terms of the vacancy acceptor level being located in the band tail. Moreover, the closeness to the LAMT quantum critical point naturally leads to an increased dielectric constant, creating a measurable Fermi surface even at very low carrier concentration. This resolves inconsistencies in historical quantum oscillation experiments<sup>46,47</sup>.

Recently, the respective Lifshitz point has also been observed by Ideue et al.<sup>17</sup> via quantum oscillation measurements. In their study, they identified three distinct transitions: one at around 5 kbar, one in the pressure range of the LAMT, and one at around 20 kbar. While we can exclude the possibility of a transition to a Weyl semimetal due to our measurements of the gap size, the measured transitions are still valid. However, we can only speculate on the origin of these transitions, and as we do not have the  $R(T)$  curves, we cannot reach a definitive conclusion.

Finally, we believe that the identification of the Anderson–Mott phase in elemental tellurium will fundamentally change our view

on the low-temperature behavior of this exciting elemental material.

## Methods

**Sample.** Transport and magnetoresistance measurements have been performed on a high-quality single crystal with 99.9999% chemical purity, purchased from Princeton Scientific<sup>TM</sup>. Sample size is  $3 \times 1 \times 0.5 \text{ mm}$ . The sample has been carefully cleaned with ethanol and, subsequently, contacts for standard 4-wire technique have been attached with Sigma Aldrich silver paint using  $25 \mu\text{m}$  platinum wires.

**Experimental set-up.** The direction of the electrical current is perpendicular to the  $c$ -axis (the screw axis of the helices), which is parallel to the external magnetic field for magnetoresistance measurements. The sample was installed in a hydrostatic piston cylinder pressure cell with a 1:1 mixture of Fluorinert<sup>TM</sup> FC77/FC70 as the pressure transferring medium. As a low-temperature pressure gauge, we used a piece of lead and monitored the development of the superconducting transition. Simultaneously, a manganin wire, installed within the cell, was used to estimate the applied pressure at room temperature. The cell was cooled, using two different adiabatic demagnetization refrigerators (ADRs) with base temperatures of 50 mK (at CBPF in Rio de Janeiro) and 250 mK (at the Cavendish Laboratory in Cambridge), respectively.

**Hall measurements.** Hall measurements have been performed on a separate piece of the sample in a Quantum Design Dynacool at ambient pressure. The sample was installed in the same manner as the main piece of the sample. The measured Hall coefficient turned out to be  $6 \times 10^{14} \text{ cm}^{-3}$  at 3 K (data included in Supplementary Fig. 2). However, as we also argue at the end of the discussion section, we do not deem this number as being particularly reliable, as recent measurements by Rikken<sup>2</sup> suggest that the Hall response of tellurium might be misleading, due to non-trivial magnetoelectric effects.

**DFT calculations.** DFT calculations were performed in the generalized gradient approximation (GGA) of the exchange-correlation effect. The QUANTUMESPRESSO package<sup>49</sup> was used with ultrasoft Perdew–Burke–Ernzerhof pseudopotentials. First, we relax the cell dimension and atomic positions of a hexagonal crystal structure for each target pressure using a tellurium scalar relativistic pseudopotential since noncollinear stress for GGA is not implemented in QUANTUMESPRESSO package. In this calculation, we used a plane-wave cutoff energy of 35 Ry and  $3 \times 3 \times 4$  Monkhorst–Pack  $k$ -point grid until a 0.1 kbar tolerance. With the optimum geometric parameters that we get for each pressure, we did a self-consistent calculation in a very dense grid of  $24 \times 24 \times 32$  Monkhorst–Pack  $k$ -points and a plane-wave cutoff energy of 50 Ry, using full relativistic pseudopotential and considering the SOC. After that we compute the band structures and the spin texture in the small, but even more dense grid, with  $37 \times 37 \times 33$   $k$ -points in the vicinity of the H point.

For the specific calculations, giving the results in Fig. 3, we relax the tellurium hexagonal Bravais-lattice structure without the SOC, varying the target pressure from  $-20$  kbar to the  $+20$  kbar. For each step of 5 kbar, we extract the in-plane and out-of-plane lattice parameters,  $a$  and  $c$ , respectively, as well as the internal atomic position parameter  $u$ , as shown in Fig. 3a and b, (with  $|a_1| = |a_2| = a$ ). After that, we included the SOC in a self-consistence calculation for each set of geometric parameters, to compute the VB structures (Fig. 3b–d) and the two-dimensional spin texture (Fig. 3f–h). We see that an equivalent pressure of  $-20$  kbar reproduces the well know “camel-back-shape” (CBS) of the VB structure along of the the K–H–K direction of the Brillouin zone<sup>14</sup>, as shown in Fig. 3c, with minimum at the H point (see Fig. 3g) for the special points and reciprocal lattice vectors). On the other hand, for a pressure of  $+10$  kbar, the CBS vanishes and the VB assumes a “dromedary-like shape” (DLS), as one can see in Fig. 3g. We assume that the transition between the CBS and DLS cases occurs at an equivalent pressure of  $-5$  kbar, where a small local minimum can still be seen at the H point. Further information on the specific calculations can be found in the Supplementary Note 1.

## Data availability

The raw data sets are available from the corresponding authors upon reasonable request.

## Code availability

The code for the DFT calculations is available from author M.M. upon reasonable request.

Received: 11 May 2020; Accepted: 26 November 2020;  
Published online: 04 January 2021



## References

- Zhang, N. et al. Magnetotransport signatures of Weyl physics and discrete scale invariance in the elemental semiconductor tellurium. *PNAS* **117**, 11337–11343 (2020).
- Rikken, G. L. J. A. & Avarvari, N. Strong electrical magnetochiral anisotropy in tellurium. *Phys. Rev. B* **99**, 245153 (2019).
- Lin, S. et al. Tellurium as a high-performance elemental thermoelectric. *Nat. Commun.* **7**, 10287 (2016).
- Gao, Z., Liu, G. & Ren, J. High thermoelectric performance in two-dimensional tellurium: an ab initio study. *ACS Appl. Mater. Interfaces* **10**, 40702–40709 (2018).
- Qin, J. et al. Raman response and transport properties of tellurium atomic chains encapsulated in nanotubes. *Nat. Electron.* **3**, 141–147 (2020).
- Furukawa, T., Shimokawa, Y., Kobayashi, K. & Itou, T. Observation of current-induced bulk magnetization in elemental tellurium. *Nat. Commun.* **8**, 954 (2017).
- Doi, T., Nakao, K. & Kamimura, H. The valence band structure of tellurium. i. The k-p perturbation method. *J. Phys. Soc. Jpn.* **28**, 36–43 (1970).
- Sakano, M. et al. Radial spin texture in elemental tellurium with chiral crystal structure. *Phys. Rev. Lett.* **124**, 136404 (2020).
- Skadron, P. & Johnson, V. A. Anisotropy and annealing behavior in extrinsic single-crystal tellurium. *J. Appl. Phys.* **37**, 1912 (1966).
- Takita, K., Hagiwara, T. & Tanaka, S. Galvanomagnetic effects in p-type tellurium at low temperatures. I. *J. Phys. Soc. Jpn.* **31**, 1469–1478 (1971).
- Phahle, A. Electrical properties of thermally evaporated tellurium films. *Thin Solid Films* **41**, 235–241 (1977).
- Anzin, V. B., Eremets, M. I., Kosichkin, Y. V., Nadezhdinski, A. I. & Shiroko, A. M. Measurement of the energy gap in tellurium under pressure. *Phys. Status Solidi (a)* **42**, 385 (1977).
- Anzin, V. B. et al. Transformation of tellurium valence band induced by hydrostatic pressure. *Phys. Status Solidi (b)* **48**, 531 (1971).
- Agapito, L. A., Kioussis, N., Goddard, W. A. & Ong, N. P. Novel family of chiral-based topological insulators: elemental tellurium under strain. *Phys. Rev. Lett.* **110**, 176401 (2013).
- Hirayama, M., Okugawa, R., Ishibashi, S., Murakami, S. & Miyake, T. Weyl node and spin texture in trigonal tellurium and selenium. *Phys. Rev. Lett.* **114**, 206401 (2015).
- Shchennikov, V. V. Magnetoresistance and thermopower of tellurium at high pressures up to 30 GPa. *Phys. Solid State* **42**, 641–647 (2000).
- Ideue, T. et al. Pressure-induced topological phase transition in noncentrosymmetric elemental tellurium. *Proc. Natl Acad. Sci. USA* <https://www.pnas.org/content/116/51/25530>. <https://www.pnas.org/content/116/51/25530.full.pdf> (2019).
- Belitz, D. & Kirkpatrick, T. R. The Anderson–Mott transition. *Rev. Mod. Phys.* **66**, 261–380 (1994).
- Enderlein, C. et al. Anomaly close to an electronic topological semimetal–insulator transition in elemental fcc-Yb under pressure. *J. Appl. Phys.* **114**, 143711 (2013).
- Xiang, Z. J. et al. Pressure-induced electronic transition in black phosphorus. *Phys. Rev. Lett.* **115**, 186403 (2015).
- Champness, C. H. & Kipling, A. L. Transport measurements in annealed single crystal tellurium. *Can. J. Phys.* **48**, 3038–3046 (1970).
- Koma, A., Tani, T. & Tanaka, S. Electrical properties of tellurium under hydrostatic pressure. I. Effects on its effective mass and energy gap. *Phys. Status Solidi (b)* **66**, 669–677 (1974).
- Delahaye, J., Brison, J. P. & Berger, C. Evidence for variable range hopping conductivity in the ordered quasicrystal i-AlPdRe. *Phys. Rev. Lett.* **81**, 4204–4207 (1998).
- Sefat, A. S. et al. Anderson–Mott transition induced by hole doping in Nd<sub>1-x</sub>TiO<sub>3</sub>. *Phys. Rev. B* **74**, 104419 (2006).
- Ying, T. et al. Anderson localization of electrons in single crystals: Li<sub>x</sub>Fe<sub>2</sub>Se<sub>8</sub>. *Sci. Adv.* **2**, <https://advances.sciencemag.org/content/2/2/e1501283>. <https://advances.sciencemag.org/content/2/2/e1501283.full.pdf> (2016).
- Tiwaria, A., Jin, C. & Narayan, J. Electrical transport in ZnO<sub>1-δ</sub> films: transition from band-gap insulator to Anderson localized insulator. *J. Appl. Phys.* **96**, 3827 (2004).
- Averkiv, N., Berezovets, V., Farbshtein, I. & Maruha, C. Antilocalization in 3d tellurium and the role of intervalley scattering in the ‘frozen’ phonon mode. *Solid State Commun.* **147**, 46–48 (2008).
- Waffenschmidt, S., Pfliederer, C. & Löhneysen, H. v. Critical behavior of the conductivity of SiP at the metal–insulator transition under uniaxial stress. *Phys. Rev. Lett.* **83**, 3005–3008 (1999).
- Altshuler, B. L. & Aronov, A. G. Theory of disordered metals and highly doped semiconductors. *Zh. Eksp. Teor. Fiz.* **77**, 2028–2044 (1979).
- Rosenbaum, T. F. et al. Metal–insulator transition in a doped semiconductor. *Phys. Rev. B* **27**, 7509–7523 (1983).
- Mott, N. F. Conduction in non-crystalline materials. *Philos. Mag.* **19**, 835–852 (1969).
- Ambegaokar, V., Halperin, B. I. & Langer, J. S. Hopping conductivity in disordered systems. *Phys. Rev. B* **4**, 2612–2620 (1971).
- Efros, A. L. & Shklovskii, B. I. *Electronic Properties of Doped Semiconductors* Vol. 45 (Springer Series in Solid-State Sciences, 1984).
- Rosenbaum, T. F. *The Disordered Insulator: Electron Glasses and Crystals*. (Springer (Institute for Amorphous Studies Series), 1985).
- Li, P. & Appelbaum, I. Intrinsic two-dimensional states on the pristine surface of tellurium. *Phys. Rev. B* **97**, 201402 (2018).
- Schmeltzer, D. & Kaveh, M. Anderson transition in the presence of the spin-orbit interaction: a crossover calculation. *Phys. Rev. B* **36**, 6698–6700 (1987).
- Kaveh, M. & Mott, N. F. Effect of spin–orbit interaction on the metal–insulator transition in doped silicon. *Philos. Mag. Lett.* **56**, 97–102 (1987).
- Zvyagin, I. P. The temperature dependence of the conductivity near the localization threshold. *Phys. Status Solidi (b)* **120**, 503–509 (1983).
- Altshuler, B. & Aronov, A. Electron–electron interaction in disordered conductors. In *Electron–electron Interactions in Disordered Systems*, Vol. 10 (eds Efros, A. & Pollak, M.) Ch. 1, 1–153 (Elsevier, 1985).
- Götte, W. A theory for the conductivity of a fermion gas moving in a strong three-dimensional random potential. *J. Phys. C* **12**, 1279–1296 (1979).
- Kawabata, A. Theory of negative magnetoresistance I. Application to heavily doped semiconductors. *J. Phys. Soc. Jpn.* **49**, 628–637 (1980).
- Ghantmakher, V. *Electrons and Disorder in Solids* (Clarendon Press, Oxford, 2005).
- Entin-Wohlman, O., Imry, Y. & Sivan, U. Orbital magnetoconductance in the variable-range-hopping regime. *Phys. Rev. B* **40**, 8342–8348 (1989).
- Baxter, D. V., Richter, R., Trudeau, M. L., Cochrane, R. W. & Strom-Olsen, J. O. Fitting to magnetoresistance under weak localization in three dimensions. *J. Phys. Fr.* **50**, 1673–1688 (1989).
- Bammes, P., Klucker, R., Koch, E. E. & Tuomi, T. Anisotropy of the dielectric constants of trigonal selenium and tellurium between 3 and 30 eV. *Phys. Status Solidi (b)* **49**, 561–570 (1972).
- Bresler, M., Farbstein, I., Mashovets, D., Kosichkin, Y. & Veselago, V. Experimental determination of the shape of the hole fermi surface in tellurium. *Physics Letters A* **29**, 23–24 (1969).
- von Klitzing, K. & Landwehr, G. Surface quantum states in tellurium. *Solid State Commun.* **9**, 2201–2205 (1971).
- Becker, W., Fuhs, W. & Stuke, J. Influence of hydrostatic pressure on the electrical conductivity of tellurium single crystals. *Phys. Status Solidi (b)* **44**, 147–154 (1971).
- Giannozzi, P. et al. QUANTUM ESPRESSO: a modular and open-source software project for quantum simulations of materials. *J. Phys.: Condens. Matter* **21**, 395502 (2009).

## Acknowledgements

C.E. would like to thank ICAM for financial support during the beginning of the project and H. Stülpner for providing material. J.F.O. would like to thank CNPq for the doctoral fellowship and specifically the CNPq/Science without borders program. This work has been made possible by financial support from FAPERJ, CNPq, and the Royal Society. E.B.-S. acknowledges support from FAPERJ through several grants including Emeritus Professor fellowship. She also thanks CNPq for BPA and corresponding grants as well as for Universal grant 425936-2016-3. S.E.R. acknowledges support from the Royal Society.

## Author contributions

J.F.O. performed most of the experimental work with support of M.B.F., S.E.R., and C.E. Most of the fundamental discussions concerning the deeper understanding of the data occurred between J.F.O., M.B.S.N., and C.E. The DFT calculations were performed by M.M., while M.B.S.N. developed the theory and performed the non-DFT computations. E.B.-S. and C.E. supervised the research. C.E. conceived of the presented idea. All authors discussed the results and contributed to the final manuscript.

## Competing interests

The authors declare no competing interests.

## Additional information

Supplementary information is available for this paper at <https://doi.org/10.1038/s43246-020-00110-1>.

Correspondence and requests for materials should be addressed to J.F.O. or C.E.

Peer review information Primary handling editor: Aldo Isidori

Reprints and permission information is available at <http://www.nature.com/reprints>

Publisher's note Springer Nature remains neutral with regard to jurisdictional claims in published maps and institutional affiliations.



**Open Access** This article is licensed under a Creative Commons Attribution 4.0 International License, which permits use, sharing, adaptation, distribution and reproduction in any medium or format, as long as you give appropriate credit to the original author(s) and the source, provide a link to the Creative Commons license, and indicate if changes were made. The images or other third party material in this article are included in the article's Creative Commons license, unless indicated otherwise in a credit line to the material. If material is not included in the article's Creative Commons license and your intended use is not permitted by statutory regulation or exceeds the permitted use, you will need to obtain permission directly from the copyright holder. To view a copy of this license, visit <http://creativecommons.org/licenses/by/4.0/>.

© The Author(s) 2021